J. Fluid Mech. (2017), *vol.* 819, *pp.* 58–103. © Cambridge University Press 2017
doi:10.1017/jfm.2017.164

Direct numerical simulation of scalar transport in turbulent flows over progressive surface waves

Di Yang[1] **and Lian Shen**[2,†]

[1]Department of Mechanical Engineering, University of Houston, Houston, TX 77204, USA

[2]Department of Mechanical Engineering and St. Anthony Falls Laboratory, University of Minnesota, Minneapolis, MN 55455, USA

(Received 2 July 2016; revised 7 March 2017; accepted 11 March 2017)

The transport of passive scalars in turbulent flows over progressive water waves is studied using direct numerical simulation. A combined pseudo-spectral and finite-difference scheme on a wave-surface-fitted grid is used to simulate the flow and scalar fields above the wave surface. Three representative wave ages (i.e. wave-to-wind speed ratios) are considered, corresponding to slow, intermediate and fast wind-waves, respectively. For each wave condition, four Schmidt numbers are considered for the scalar transport. The presence of progressive surface waves is found to induce significant wave-phase-correlated variation to the scalar field, with the phase dependence varying with the wave age. The time- and plane-averaged profiles of the scalar over waves of various ages exhibit similar vertical structures as those found in turbulence over a flat wall, but with the von Kármán constant and effective wave surface roughness for the mean scalar profile exhibiting considerable variation with the wave age. The profiles of the root-mean-square scalar fluctuations and the horizontal scalar flux exhibit good scaling in the viscous sublayer that agrees with the scaling laws previously reported for flat-wall turbulence, but with noticeable wave-induced variation in the viscous wall region. The profiles of the vertical scalar flux in the viscous sublayer exhibit apparent discrepancies from the reported scaling law for flat-wall turbulence, due to a negative vertical flux region above the windward face of the wave crest. Direct observation and quadrant-based conditional averages indicate that the wave-dependent distributions of the scalar fluctuations and fluxes are highly correlated with the coherent vortical structures in the turbulence, which exhibit clear wave-dependent characteristics in terms of both shape and preferential location.

Key words: turbulent boundary layers, turbulence simulation, wind–wave interactions

1. Introduction

The air–sea exchange of scalar quantities, such as water vapour and heat, near the air–water interface plays a vital role in global and regional air–sea interactions (Smith 1988; DeCosmo *et al.* 1996; Fairall *et al.* 1996; Edson *et al.* 2007). Turbulent transport of scalars in the air above the sea surface is strongly affected by the

† Email address for correspondence: shen@umn.edu

surface waves. The periodical surface curvatures and the motions of these waves can induce considerable disturbance to the air turbulent flows near the wave surface, affecting the transport of both momentum and scalars (Edson *et al.* 2007; Sullivan & McWilliams 2010).

Various experimental studies have been conducted in the past several decades to characterize the effect of sea-surface waves on air–sea scalar transport. For example, Fairall *et al.* (1996), Bourassa, Vincent & Wood (1999) and Edson *et al.* (2004) measured the bulk properties of the air–sea scalar exchange, and parameterized the scalar flux profiles in terms of averaged air–sea interfacial properties such as the scalar transfer coefficient, sea-surface scalar roughness length, and convective scaling velocity. Edson *et al.* (2007) measured the velocity, temperature and relative humidity in the marine atmospheric boundary layer (ABL) under low winds in the CBLAST-LOW experiment. Based on the CBLAST-LOW data, Katsouvas, Helmis & Wang (2007) performed quadrant analysis for the scalar and momentum fluxes. Katul, Sempreviva & Cava (2008) analyzed the data from RASEX (Risø Air Sea EXperiment) and developed a one-dimensional model for the temperature–humidity covariance. Experimental studies of air–sea scalar transport have provided valuable insights and parameterizations for modelling air–sea interactions.

In recent years, enabled by the continuous advancement of computer power, numerical simulation has become a valuable tool for studying the fine-scale scalar transport phenomena near the air–water interface. Modelling the air turbulence over sea surfaces is challenging, primarily due to the difficulty associated with modelling the effect of sea-surface waves. One approach is to approximate the marine ABL as turbulence over a flat surface, with the wave effect parameterized as the sea-surface roughness length (e.g. Charnock 1955; Fairall *et al.* 1996). However, accurately parameterizing the sea-surface roughness is found to be quite challenging due to the complexity in wind–wave interaction (e.g. Donelan 1990; Toba, Smith & Ebuchi 2001; Yang, Meneveau & Shen 2013). Instead, many previous numerical studies attempted to directly simulate air turbulence over progressive surface waves, with the instantaneous wave motions imposed in the simulation as bottom boundary conditions (e.g. Sullivan, McWilliams & Moeng 2000; Sullivan & McWilliams 2002; Kihara *et al.* 2007; Yang & Shen 2009, 2010; Druzhinin, Troitskayaa & Zilitinkevich 2016). Most of these previous studies focused on the momentum transfer between the air turbulence and the water waves. Sullivan & McWilliams (2002) and Druzhinin *et al.* (2016) considered the temperature field in their simulations with a Prandtl number of 0.7, corresponding to the ratio of kinematic viscosity to thermal diffusivity of the air, and studied the effects of various stratification conditions (characterized by the Richardson number) on the characteristics of the air turbulence. On the other hand, a number of numerical studies have been performed focusing on the statistics of scalar fluctuations over stationary wavy walls (e.g. Antonia & Kim 1991; Kawamura *et al.* 1998; Dellil, Azzi & Jubran 2004; Park, Choi & Suzuki 2004; Choi & Suzuki 2005; Rossi 2010). These studies have shown significant effects of the stationary waves on the characteristics of scalar transport, such as the surface scalar flux, the mean scalar concentration, the scalar variance and the turbulent scalar fluxes. However, there is still a lack of studies devoted to the mechanism of scalar transport in turbulence over progressive surface waves, which is expected to be significantly different from the cases with stationary wavy walls (Belcher & Hunt 1998; Sullivan & McWilliams 2010).

In this study, the direct numerical simulation (DNS) solver developed by Yang & Shen (2011*a*) is adopted, which uses a boundary-fitted computational grid system

that follows the instantaneous wave surface elevation and motions, allowing one to resolve the details of the turbulent flow above and in the vicinity of the mobile wave surface. In the present study, this DNS solver is further expanded by including a scalar transport solver within the boundary-fitted spatial discretization framework, and is used to simulate the transport of passive scalars in turbulent flows over progressive surface waves. As in many recent numerical studies, a plane progressive surface wave train is imposed at the bottom of the simulation domain (e.g. Sullivan *et al.* 2000, 2008; Sullivan & McWilliams 2002; Kihara *et al.* 2007; Yang & Shen 2009, 2010; Hara & Sullivan 2015; Druzhinin *et al.* 2016). A relatively large wave steepness of $ak = 0.25$ is considered, where a is the wave amplitude and k is the wavenumber. To account for the nonlinearity associated with such a steep wave, a high-order Stokes wave solution is used to prescribe the wave surface elevation and orbital velocity. Three representative wave-to-wind speed ratios c/u_* (also called the wave age) are considered, including $c/u_* = 2$ (slow waves), 14 (intermediate waves) and 25 (fast waves), where c is the wave phase speed and u_* is the friction velocity of the turbulence. In order to achieve the desired value for c/u_*, the turbulent flow is driven by a constant streamwise stress applied at the top flat boundary, and the mean flow has a Couette-flow-type of velocity profile, but with the mean velocity at the top boundary varying for different wave conditions. The scalar transport is known to be largely affected by the Schmidt number $Sc = \nu/D$, where ν is the kinematic viscosity and D is the scalar molecular diffusivity. For each wave condition, four Schmidt numbers are considered, including $Sc = 0.5$, 1.0, 2.0 and 4.0. Based on the DNS data, the effects of surface waves on the scalar transport are studied by various statistical analysis techniques, including time and plane average, wave phase average, quadrant analysis and conditional average. The correlations between coherent vortical structures and turbulent scalar transport events are also studied by direct observation of instantaneous snapshots and quadrant-based conditional averages.

The remainder of this paper is organized as follows. First, the mathematical formulas and numerical schemes of the DNS solver are described in § 2. Then the configurations of the simulation cases are given in § 3, together with some sample results of the DNS. In § 4, various types of statistical analyses of the DNS data are performed, and the effects of surface waves on the characteristics of flow structures and turbulent scalar transport are discussed. Finally, conclusions are given in § 5.

2. Description of DNS

As shown in figure 1, this study uses DNS to examine the transport of passive scalars in a three-dimensional stress-driven turbulent Couette flow over a plane progressive surface wave train. The Cartesian coordinates are denoted as $x_i(i = 1, 2, 3) = (x, y, z)$, where x and y are the horizontal coordinates and z is the vertical coordinate, with $z = 0$ being the mean elevation of the surface wave at the bottom of the simulation domain; $u_i(i = 1, 2, 3) = (u, v, w)$ are the corresponding velocity components in x-, y- and z-directions, respectively.

In the simulation, the flow is driven by a constant streamwise shear stress τ_x prescribed on the rigid flat top boundary, which prescribes a fixed turbulence friction velocity of $u_* = \sqrt{\tau_x/\rho}$, where ρ is the fluid density. The bottom of the flow is bounded and distorted by a two-dimensional wave train that propagates in the x-direction. This stress-driven Couette flow configuration has been used as a canonical problem to study the surface water wave effect on turbulent air flows in many previous numerical studies (e.g. Gent & Taylor 1976; Li, Xu & Taylor 2000;

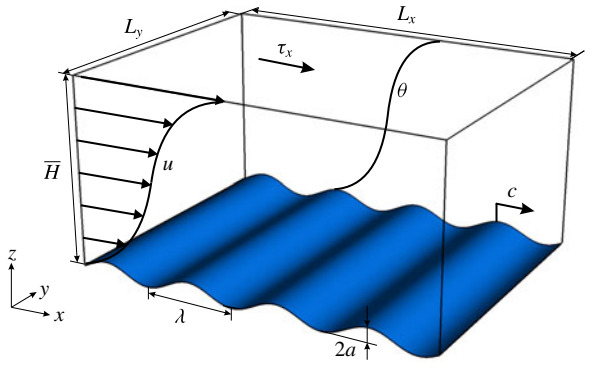

FIGURE 1. (Colour online) Sketch of the simulation configuration. A three-dimensional turbulent Couette flow is driven by a constant shear stress τ_x applied at the top boundary, and flows over a plane progressive surface wave train. The surface wave has a wavelength λ and an amplitude a. The wave propagates in the x-direction with a phase speed c. The passive scalar field θ is transported by the turbulent Couette flow, with Dirichlet boundary conditions of $\theta = 0$ and $\theta = 2$ at the bottom and top boundaries, respectively.

Kihara *et al.* 2007; Yang & Shen 2009, 2010). A passive scalar θ is transported by the turbulent flow, with a Dirichlet boundary condition of $\theta = 0$ on the bottom wave surface and $\theta = 2$ on the top boundary. This configuration for θ results in $\theta \approx 1$ at the centre of the simulation domain. We remark that in this canonical simulation configuration, we set the passive scalar to have a smaller value near the wave surface and a larger value near the upper boundary, similar to many previous numerical studies (e.g. Dellil *et al.* 2004; Park *et al.* 2004; Rossi 2010). In some applications, e.g. the moisture in the marine atmospheric boundary layer, the scalars have higher concentrations near the wave surface. Because θ is assumed to be passive and its governing equation is linear with respect to θ, the results reported in this study can be converted to the reversed configuration with a larger scalar value near the wave surface. We choose the current configuration as it allows us to compare the current DNS results to the previously reported results of passive scalar transport in turbulent boundary layers over flat and wavy boundaries.

In the DNS, the turbulent carrier flow is described by the three-dimensional incompressible Navier–Stokes equations

$$\frac{\partial u_i}{\partial x_i} = 0, \tag{2.1}$$

$$\frac{\partial u_i}{\partial t} + \frac{\partial (u_i u_j)}{\partial x_j} = -\frac{1}{\rho}\frac{\partial p}{\partial x_i} + \nu \frac{\partial^2 u_i}{\partial x_j \partial x_j}, \tag{2.2}$$

where p is the pressure. The transport of the passive scalar $\theta(x, y, z, t)$ is governed by a convection–diffusion equation

$$\frac{\partial \theta}{\partial t} + \frac{\partial (\theta u_j)}{\partial x_j} = D \frac{\partial^2 \theta}{\partial x_j \partial x_j}. \tag{2.3}$$

The effect of progressive surface waves on the turbulence is imposed through a Dirichlet velocity boundary condition at the bottom wave surface, $u_i(z = \eta) = (u_s, v_s, w_s)$, where η is the wave surface elevation and (u_s, v_s, w_s) are the wave

surface orbital velocities. In this study, we use a high-order two-dimensional Stokes wave solution to prescribe the motions of the plane-progressive surface wave train (Stokes 1847),

$$\eta(x, y, t) = \sum_{n=1}^{N} (ak)^{n-1} \eta^{(n)}(x, y, t), \tag{2.4}$$

$$u_s(x, y, t) = \sum_{n=1}^{N} (ak)^{n-1} u_s^{(n)}(x, y, t), \tag{2.5}$$

$$v_s(x, y, t) = 0, \tag{2.6}$$

$$w_s(x, y, t) = \sum_{n=1}^{N} (ak)^{n-1} w_s^{(n)}(x, y, t), \tag{2.7}$$

where the variables with superscript '(n)' indicate the nth mode of the corresponding wave quantity. In particular, following Dommermuth & Yue (1987), we directly solve the nonlinear equations associated with the mapping function in Schwartz (1974) by using Newton iteration up to a high order of $N = 192$. As a reference, the Stokes solution up to the second order can be found in Dean & Dalrymple (1991). For the purpose of defining some key parameters of the wave boundary conditions, in the following equations only the leading order mode of the Stokes wave solution is given, which is the same as the Airy wave solution and has been used in many prior DNS studies (e.g. Sullivan *et al.* 2000, 2008; Kihara *et al.* 2007; Hara & Sullivan 2015; Druzhinin *et al.* 2016):

$$\eta^{(1)}(x, y, t) = a \sin\, k(x - ct), \tag{2.8}$$

$$u_s^{(1)}(x, y, t) = akc\, \sin k(x - ct), \tag{2.9}$$

$$v_s^{(1)}(x, y, t) = 0, \tag{2.10}$$

$$w_s^{(1)}(x, y, t) = akc\, \cos k(x - ct). \tag{2.11}$$

Here, a is the amplitude of the leading wave mode, $k = 2\pi/\lambda$ is its wavenumber, λ is its wavelength, and c is its phase speed.

We note that the current DNS solver can be dynamically coupled with another solver for the water waves, allowing the simulation of turbulence with a dynamically evolving wave field (Yang & Shen 2011*b*). Because this study focuses on understanding the fundamental mechanisms of the surface wave effects on the passive scalar transport, we choose to use the canonical configuration with a prescribed Stokes wave boundary condition, which allows for a precise phase average based on the periodic wave form and yields well-converged statistics for the flow and scalar fields. Moreover, when a more realistic dynamically evolving wave field (either monochromatic or broadband) is considered, a realistically high Reynolds number should be considered in order to capture the interaction between turbulence and surface waves over a wide range of scales, for which the flow and scalar fields have to be simulated using wall-modelled large-eddy simulation (Yang *et al.* 2013; Yang, Meneveau & Shen 2014*a*,*b*). These more realistic and complicated conditions go beyond the scope of the current canonical study, but are worth considering in future studies of scalar transport in turbulent wind over ocean waves.

To capture the surface wave effect on the scalar field, the DNS solver uses a boundary-fitted coordinate system that follows the instantaneous deformation of the

wave surface. The irregular wave surface-bounded domain in the physical space (x, y, z, t) is transformed to a right rectangular prism in the computational space (ξ, ψ, ζ, τ) with the following algebraic mapping:

$$\xi = x, \quad \psi = y, \quad \zeta = \frac{z - \eta(x, y, t)}{H(x, y, t)} = \frac{z - \eta(x, y, t)}{\overline{H} - \eta(x, y, t)}, \quad \tau = t. \tag{2.12a–d}$$

Here, the height of the physical domain, $H(x, y, t)$, is decomposed into an average height $\overline{H}$ and a wave induced variation $-\eta(x, y, t)$. Similar to x_i, the spatial coordinates in the computational space can also be denoted using the index notation as $\xi_i (i = 1, 2, 3) = (\xi, \psi, \zeta)$.

The Jacobian matrix of the spatial coordinate transformation is

$$\boldsymbol{J} = \begin{bmatrix} \dfrac{\partial \xi}{\partial x} & \dfrac{\partial \xi}{\partial y} & \dfrac{\partial \xi}{\partial z} \\ \dfrac{\partial \psi}{\partial x} & \dfrac{\partial \psi}{\partial y} & \dfrac{\partial \psi}{\partial z} \\ \dfrac{\partial \zeta}{\partial x} & \dfrac{\partial \zeta}{\partial y} & \dfrac{\partial \zeta}{\partial z} \end{bmatrix} = \begin{bmatrix} 1 & 0 & 0 \\ 0 & 1 & 0 \\ \dfrac{\zeta - 1}{\overline{H} - \eta} \dfrac{\partial \eta}{\partial x} & \dfrac{\zeta - 1}{\overline{H} - \eta} \dfrac{\partial \eta}{\partial y} & \dfrac{1}{\overline{H} - \eta} \end{bmatrix}. \tag{2.13}$$

Because the wave surface oscillates in time, a transformation is also required for the temporal derivative terms, i.e.

$$\frac{\partial}{\partial t} = \frac{\partial}{\partial \tau} + \frac{\partial \zeta}{\partial t} \frac{\partial}{\partial \zeta}, \quad \text{where } \frac{\partial \zeta}{\partial t} = \frac{\zeta - 1}{\overline{H} - \eta} \frac{\partial \eta}{\partial t}. \tag{2.14}$$

By applying the chain rule together with (2.13) and (2.14), we write the governing equations (2.1)–(2.3) in the wave-surface-fitted coordinates as

$$J_{kj} \frac{\partial u_j}{\partial \xi_k} = 0, \tag{2.15}$$

$$\frac{\partial u_i}{\partial \tau} + \delta_{j3} \frac{\partial \zeta}{\partial t} \frac{\partial u_i}{\partial \xi_j} + J_{kj} \frac{\partial (u_i u_j)}{\partial \xi_k} = -\frac{J_{ki}}{\rho} \frac{\partial p}{\partial \xi_k} + \nu J_{nj} \frac{\partial}{\partial \xi_n} \left(J_{kj} \frac{\partial u_i}{\partial \xi_k} \right), \tag{2.16}$$

$$\frac{\partial \theta}{\partial \tau} + \delta_{j3} \frac{\partial \zeta}{\partial t} \frac{\partial \theta}{\partial \xi_j} + J_{kj} \frac{\partial (\theta u_j)}{\partial \xi_k} = D J_{nj} \frac{\partial}{\partial \xi_n} \left(J_{kj} \frac{\partial \theta}{\partial \xi_k} \right), \tag{2.17}$$

where J_{ij} is the index notation of the matrix $\boldsymbol{J}$ and δ_{ij} is the Kronecker delta. Note that u_i are the velocities in the physical space.

In DNS, equations (2.15)–(2.17) are discretized in the computational space (ξ, ψ, ζ, τ) and solved numerically. In particular, a Fourier-series-based pseudo-spectral method is used in the (ξ, ψ)-plane, with evenly spaced collocated grid points in both directions. The standard 2/3-rule is used for eliminating the aliasing error. In the vertical direction, a second-order finite-difference method is used based on a staggered ζ-grid. The vertical grid is clustered near the top boundary and the bottom wave surface to provide adequate resolution for the boundary layers. The governing equations are integrated in time with a fractional-step method. For both (2.16) and (2.17), the nonlinear convection terms are advanced in time using a second-order Adams–Bashforth scheme. In order to resolve the boundary layer without requiring a significantly small timestep, a semi-implicit scheme is desired for

time advancement of the viscous diffusion terms in (2.16) and (2.17). Due to the coordinate transformation (2.12), in the computational space the Laplacian operator in the diffusion terms becomes

$$\nabla^2 = J_{nj}\frac{\partial}{\partial\xi_n}\left(J_{kj}\frac{\partial}{\partial\xi_k}\right) = \underbrace{\frac{\partial^2}{\partial\xi^2}+\frac{\partial^2}{\partial\psi^2}+2J_{31}\frac{\partial^2}{\partial\xi\partial\zeta}+2J_{32}\frac{\partial^2}{\partial\psi\partial\zeta}}_{\nabla^2_{\xi\psi}} + \underbrace{\left(J_{31}^2+J_{32}^2+J_{33}^2\right)\frac{\partial^2}{\partial\zeta^2}+\left(\frac{\partial^2\zeta}{\partial x^2}+\frac{\partial^2\zeta}{\partial y^2}\right)\frac{\partial}{\partial\zeta}}_{\nabla^2_{\zeta}}, \tag{2.18}$$

where

$$\frac{\partial^2\zeta}{\partial x^2} = \frac{\zeta-1}{\overline{H}-\eta}\frac{\partial^2\eta}{\partial x^2}+\frac{2(\zeta-1)}{(\overline{H}-\eta)^2}\left(\frac{\partial\eta}{\partial x}\right)^2, \tag{2.19}$$

$$\frac{\partial^2\zeta}{\partial y^2} = \frac{\zeta-1}{\overline{H}-\eta}\frac{\partial^2\eta}{\partial y^2}+\frac{2(\zeta-1)}{(\overline{H}-\eta)^2}\left(\frac{\partial\eta}{\partial y}\right)^2. \tag{2.20}$$

In the Laplacian operator (2.18), the first part, $\nabla^2_{\xi\psi}$, involves derivatives with respect to ξ and ψ, and is thus treated with the second-order Adams–Bashforth scheme; the second part, ∇^2_{ζ}, is treated semi-implicitly using the Crank–Nicolson scheme. Note that if the Crank–Nicolson scheme is used for the entire diffusion term and if the momentum equations are solved by the pseudo-spectral method, the presence of the several Jacobian coefficients J_{ij} in (2.18) would require (2.16) and (2.17) to be solved iteratively. The use of the above hybrid scheme helps to avoid iteration, and meanwhile keeps the dominant diffusion terms $\nu\nabla^2_{\zeta}u_i$ and $D\nabla^2_{\zeta}\theta$ semi-implicit. Compared with a pure explicit scheme, this hybrid scheme relaxes the numerical stability constraint on the simulation timestep when using a refined vertical grid to adequately resolve the boundary layer. For the velocity field, the incompressibility constraint (2.15) is satisfied by constructing and solving a Poisson equation for the pressure and then adding pressure correction terms to the velocity components. Note that because of the non-constant coefficients in the Laplacian operator (2.18), the pressure Poisson equation needs to be solved iteratively.

We also remark that while (2.2) and (2.3) are written in the conservative form, after the coordinate transformation, (2.16) and (2.17) are in a weakly conservative form. A strongly conservative form can be further derived by first dividing (2.16) and (2.17) by the Jacobian and then rearranging all the terms into the forms of derivatives of the primary variables with respect to the independent variables (ξ, ψ, ζ, τ) (e.g. Vinokur 1974; Anderson, Tannehill & Pletcher 1984; Zang, Street & Koseff 1994; Sullivan *et al.* 2000). Nevertheless, the above numerical scheme is found to provide accurate results, especially for air flows over water waves, with relatively low computational cost. Extensive validation and detailed discussion on the performance of the numerical scheme can be found in Yang & Shen (2011*a*,*b*). Additional validations for turbulent flows and scalar transport over a flat wall are given in appendix A.

3. Simulation configuration

For the simulations of turbulent flows over surface waves considered in this study, the flow is driven by a constant shear stress τ_x applied on the top boundary of the

simulation domain. The Reynolds number based on the friction velocity $u_* = \sqrt{\tau_x/\rho}$ and half of the mean domain height $\delta = \overline{H}/2$ is $Re_* = u_*\delta/\nu = 445$. To capture the effect of surface waves on the turbulence transport of scalars, a computational domain of $\left(L_x, L_y, \overline{H}\right) = (4\lambda, 3\lambda, 2\lambda)$ is used, where the wavelength $\lambda = \delta$. This domain size has been found to be sufficiently large based on the test of two-point spatial correlation (Yang & Shen 2009). The domain is transformed into the computational space (ξ, ψ, ζ) based on (2.12), and then discretized using 192^3 grid points. In particular, the grid points are evenly spaced in the ξ- and ψ-directions, providing grid resolutions of $\Delta\xi^+ = 9.27$ and $\Delta\psi^+ = 6.95$, respectively (here the subscript '+' denotes the length in wall unit, i.e. normalized by ν/u_*). In the vertical direction, the grid points are clustered near the bottom and top boundaries with $\Delta\zeta^+ = 0.4$, and become coarsely spaced towards the centre of the domain with $\Delta\zeta^+ = 8.7$.

Note that the Reynolds number considered in the current DNS study is lower than those used in DNS studies of turbulence over a flat surface (e.g. Hoyas & Jiménez 2006; Lee & Moser 2015) because of the additional complexity and computational cost caused by the boundary-fitted grid and coordinate transformation, but is higher than those used in many previous DNS studies of turbulence over progressive and stationary waves, e.g. $Re_* = 171$ in De Angelis, Lombardi & Banerjee (1997), $Re_* = 100 \sim 164$ in Sullivan *et al.* (2000) and Sullivan & McWilliams (2002), $Re_* = 150$ in Kihara *et al.* (2007), $Re_* = 283$ in Yang & Shen (2010), and $Re_* = 140 \sim 325$ in Druzhinin, Troitskaya & Zilitinkevich (2012) and Druzhinin *et al.* (2016). Although limited to relatively low Reynolds numbers, DNS has been found to be able to reproduce many key features of laboratory experiments and field observations (Sullivan & McWilliams 2010). More importantly, DNS directly resolves the flow and scalar transport in the near-surface region, where molecular viscosity and diffusivity play an important role. Meirink & Makin (2000) solved the Reynolds-averaged Navier–Stokes equations using a Dirichlet wave boundary condition and a second-order closure of Craft & Launder (1996) that is valid in the viscous sublayer, and reproduced the air flow over water waves measured by Stewart (1970), suggesting the importance of capturing the viscous effect when modelling wind–wave interaction (Sullivan & McWilliams 2010).

Because DNS usually uses relatively low Reynolds numbers to resolve all the essential turbulence motions at different scales, the velocity and length scales considered in the present and other similar studies in literature do not directly match the real scales in wind over water waves. Nevertheless, DNS has been proven to provide valuable insights for understanding the characteristics of wind turbulence over waves. Moreover, previous studies have shown that the wave age, defined as the ratio of the wave phase speed c to a characteristic wind velocity, is a key parameter for the quantitative description of wind–wave interaction (see the reviews by Belcher & Hunt 1998; Sullivan & McWilliams 2010). Typical choices of the characteristic wind velocity include: (1) the wind friction velocity, u_* (e.g. Belcher & Hunt 1998; Sullivan *et al.* 2000; Kihara *et al.* 2007; Yang & Shen 2009, 2010); (2) the mean wind velocity at a height proportional to the wavelength λ, e.g. U_λ at $z = \lambda$ or $U_{\lambda/2}$ at $z = \lambda/2$ (e.g. Sullivan *et al.* 2000; Donelan *et al.* 2006); and (3) the mean wind velocity at a fixed height above the mean wave surface regardless of the wavelength, e.g. U_{10} at the 10 m height (see, e.g., Hristov, Miller & Friehe 2003; Donelan *et al.* 2006, among others). In this study, because the carrier flow is driven by a prescribed stress τ_x that gives a constant friction velocity u_*, it is most convenient to define the wave age as c/u_*.

To study the effect of surface wave motion on the scalar transport, three different wave ages are considered, $c/u_* = 2$, 14 and 25, corresponding to the young,

Case	Type	c/u_*	κ	z_0^+	B	Sc	κ_θ	$z_{0,\theta}^+$	B_θ
S25	stationary	0	0.43	1.21	−0.44	0.5	0.48	1.22	−0.41
	sinusoidal					1.0	0.48	2.09×10^{-1}	3.27
	wave					2.0	0.48	1.54×10^{-2}	8.72
						4.0	0.48	3.09×10^{-4}	17.01
W25C2	Stokes wave	2	0.39	2.31	−2.17	0.5	0.43	1.89	−1.46
						1.0	0.42	4.69×10^{-1}	1.79
						2.0	0.41	6.35×10^{-2}	6.64
						4.0	0.41	3.27×10^{-3}	14.08
W25C14	Stokes wave	14	0.39	0.22	3.84	0.5	0.46	7.06×10^{-1}	0.75
						1.0	0.46	8.49×10^{-2}	5.42
						2.0	0.45	3.46×10^{-3}	12.63
						4.0	0.44	2.82×10^{-5}	23.97
W25C25	Stokes wave	25	0.27	0.55	2.24	0.5	0.35	1.76	−1.60
						1.0	0.33	3.91×10^{-1}	2.81
						2.0	0.31	4.52×10^{-2}	9.85
						4.0	0.29	2.14×10^{-3}	21.40

TABLE 1. List of DNS cases for turbulent flow over stationary and Stokes waves with steepness $ak = 0.25$ and Reynolds number $Re_* = 445$. In the table, the parameters without and with subscript 'θ' are for mean velocity and scalar profiles, respectively. In particular, κ is the von Kármán constant, z_0^+ is the effective wave surface roughness, and B is the profile offset. Detailed discussions of the mean profiles are given in § 4.3.

intermediate and mature stages of wind-generated waves, respectively (Belcher & Hunt 1998). Moreover, if $c = 0$, the bottom boundary becomes a stationary wavy wall without orbital motion, which has often been used as a reference case for comparison in many prior numerical studies of flows over surface waves. All of the four wave cases have a wave steepness of $ak = 0.25$. The wave cases considered in the present study are summarized in table 1. For each wave case, four Schmidt numbers, $Sc = 0.5$, 1.0, 2.0 and 4.0, are considered in the DNS for the scalar transport. Figure 2 shows some sample DNS results for the instantaneous scalar concentration field in turbulence over the four different types of waves with $Sc = 1.0$. Apparent differences in the instantaneous scalar field can be observed among the stationary (S25), slow (W25C2) and intermediate (W25C14) wave cases, while the difference between the intermediate and fast (W25C25) wave cases is less obvious. To quantitatively study the effect of surface waves on scalar transport, in the next section various statistical analyses are performed for the scalar field. For data sampling, in all the cases the simulations were carried out for approximately 34 000 viscous time units (i.e. tu_*^2/ν). Three-dimensional snapshots of instantaneous velocity and scalar fields were outputted for every 20 viscous time units starting from approximately 26 000 viscous time units, with totally 400 instantaneous snapshots sampled for the statistical analyses.

4. Results

4.1. *Phase-averaged scalar field*

To quantify the effect of surface waves on the turbulent flow and scalar fields, a triple decomposition is applied to analyze the instantaneous quantities. Specifically, an instantaneous quantity $f(x, y, z, t)$ obtained from the DNS can be decomposed as (e.g.

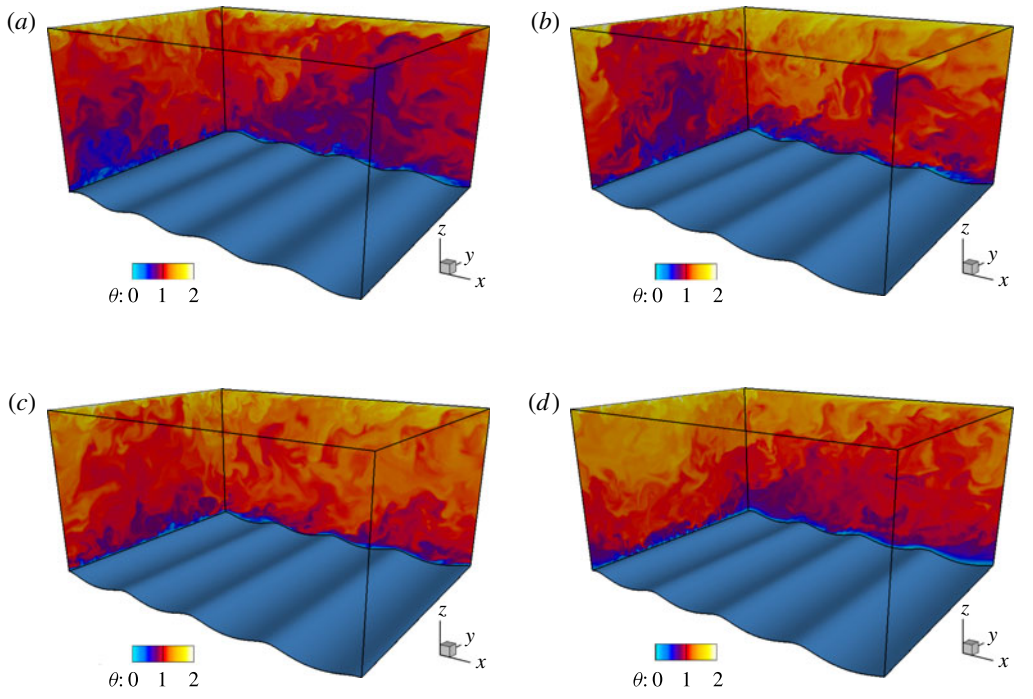

FIGURE 2. (Colour online) Three-dimensional illustration of instantaneous scalar field in turbulence over surface waves for various wave cases: (*a*) S25 (stationary wave); (*b*) W25C2 (slow wave); (*c*) W25C14 (intermediate wave); and (*d*) W25C25 (fast wave). For all cases, the contours of the instantaneous scalar concentration θ for $Sc = 1.0$ are shown on the two representative vertical planes. The wave surface is shaded blue for illustrative purposes. In (*b–d*), the waves propagate in the x-direction.

Sullivan *et al.* 2000; Kihara *et al.* 2007; Yang & Shen 2010)

$$f(x, y, z, t) = \langle f\rangle(x, z) + f'(x, y, z, t) = \overline{f}(\zeta) + \widetilde{f}(x, z) + f'(x, y, z, t), \tag{4.1}$$

where $\langle f\rangle$ denotes the phase average, $\overline{f}$ denotes the time and ζ-plane average over all (ξ, ψ, τ) in the computational space (hereinafter simply referred to as the time and plane average), $\widetilde{f}$ denotes the wave-induced variation of f, and f' denotes the instantaneous fluctuation. In particular, the phase average $\langle f\rangle$ is calculated by shifting the instantaneous quantity f to the same phase with respect to the surface wave, then averaging in time and along the spanwise direction, and lastly further averaging among the four streamwise waves (Yang & Shen 2010). The wave-induced variation is then obtained by subtracting from the phase average the time and plane average at the corresponding ζ level in the computational space, i.e. $\widetilde{f}(x, z) = \langle f\rangle(x, z) - \overline{f}(\zeta)$. As a result of the averaging among the four different waves, only one wavelength is necessary when presenting $\langle f\rangle$ and $\widetilde{f}$. Moreover, when presenting the vertical profile of the time and plane average $\overline{f}$, the ζ coordinate is converted to the physical coordinate above the wave surface as $\overline{z} = \overline{H}\zeta$ (for a flat-surface case, $\overline{z} = z$). Hereinafter, for simplification $\overline{f}$ is also referred to as the mean of f.

Note that to calculate the mean, one could also choose to first interpolate the physical quantities obtained from the boundary-fitted DNS to a regular Cartesian

grid and then average on planes of constant z. However, by doing so the flow region below the height of the wave crest would be excluded (e.g. Rutgersson & Sullivan 2005). As shown in the following subsections, because the current DNS uses boundary-fitted grid with the ζ-plane nearly parallel to the wave surface near the lower boundary (see figure 29*a* in appendix B), calculating $\bar{f}$ by averaging on planes of constant ζ allows us to capture the linear profiles of mean velocity and scalar in the thin viscous sublayer very close to the wave surface. Meanwhile, in the log-law region the difference of the mean profiles obtained by averaging on z planes and ζ planes is found to be small because the ζ plane becomes flatter as ζ increases (see more information in appendix B). Moreover, defining and calculating $\bar{f}$ based on ζ allows us to have meaningful values for the wave-correlated variation $\tilde{f}$ in the entire phase-averaged domain, including the region above the trough but below the elevation of the crest. Similar triple decomposition approaches as (4.1) have been used in previous studies of turbulent flows over waves (e.g. Sullivan *et al.* 2000; Sullivan & McWilliams 2002; Kihara *et al.* 2007; Hara & Sullivan 2015).

Figure 3 shows the phase-averaged streamlines and scalar concentration $\langle\theta\rangle$ for various wave cases. The streamlines are plotted based on the velocity vector $(\langle u\rangle - c, \langle w\rangle)$, representing the mean flow pattern in the wave-following reference frame. In case S25 (figure 3*a*), due to the large amplitude of the stationary wavy surface, the phase-averaged flow separates on the leeward face of the crest and reattaches on the windward face of the succeeding crest. The streamlines in the separation zone exhibit a closed-circle pattern, which does not extend vertically beyond the elevation of the wave crest. Above the separation zone, the streamlines are nearly horizontal, with a slightly concave curvature above the reattachment region. The distribution of the phase-averaged scalar concentration $\langle\theta\rangle$ exhibits correlation with the streamline patterns (figure 3*b*). Near the wavy surface, the low-$\langle\theta\rangle$ region is lifted up in the separation zone between the crest and the succeeding trough (i.e. roughly between $x/\lambda = 0.1$ and 0.5) due to the mean upward flow motion associated with the separation, resulting in a reduced vertical gradient for $\langle\theta\rangle$; near the reattachment zone (i.e. around $x/\lambda = 0.7$), the mean flow sweeps towards the windward face of the succeeding crest, resulting in a strong near-surface shear layer (from $x/\lambda = 0.6$ to 1.0) with a high vertical gradient for both $\langle u\rangle$ and $\langle\theta\rangle$. These wave-phase-dependent modulations of the near-surface distribution of $\langle\theta\rangle$ are revisited when the Sherwood number Sh is discussed in the next section (§ 4.2). Above the elevation of the crest, the contour lines of $\langle\theta\rangle$ become nearly horizontal, consistent with the horizontal streamlines at these high elevations. Similar near-surface modulation of $\langle\theta\rangle$ has also been reported in the DNS study by Rossi (2010) for transport of a scalar with $Sc = 0.7$ in a turbulent channel flow over a stationary wavy surface with steepness $ak = 0.314$. Figure 4 shows a corresponding case obtained from our DNS (with $ak = 0.314$ and $Re_* = 283$), which yields reasonably good agreement with the DNS results from Rossi (2010).

In case W25C2 (figure 3*c*,*d*), the wave surface has non-zero orbital velocities (u_s, w_s) that induce additional distortion to the flow field above it (in addition to the boundary curvature effect as in case S25). In the reference frame that moves with the wave at its phase speed c, near the surface the mean streamwise velocity $\langle u\rangle - c$ is in the $-x$-direction. As $\langle u\rangle$ increases with height, $\langle u\rangle - c$ becomes zero at the height indicated by the dash-dot line in figure 3(*c*), and becomes positive further above. The layer where $\langle u\rangle - c = 0$, known as the 'critical layer', was found to play a crucial role in the momentum transfer between the turbulence and the surface waves (e.g. Miles 1957; Lighthill 1962; Sullivan *et al.* 2000; Hristov *et al.* 2003). Around the critical layer, the streamlines form a closed-circle pattern, named as the

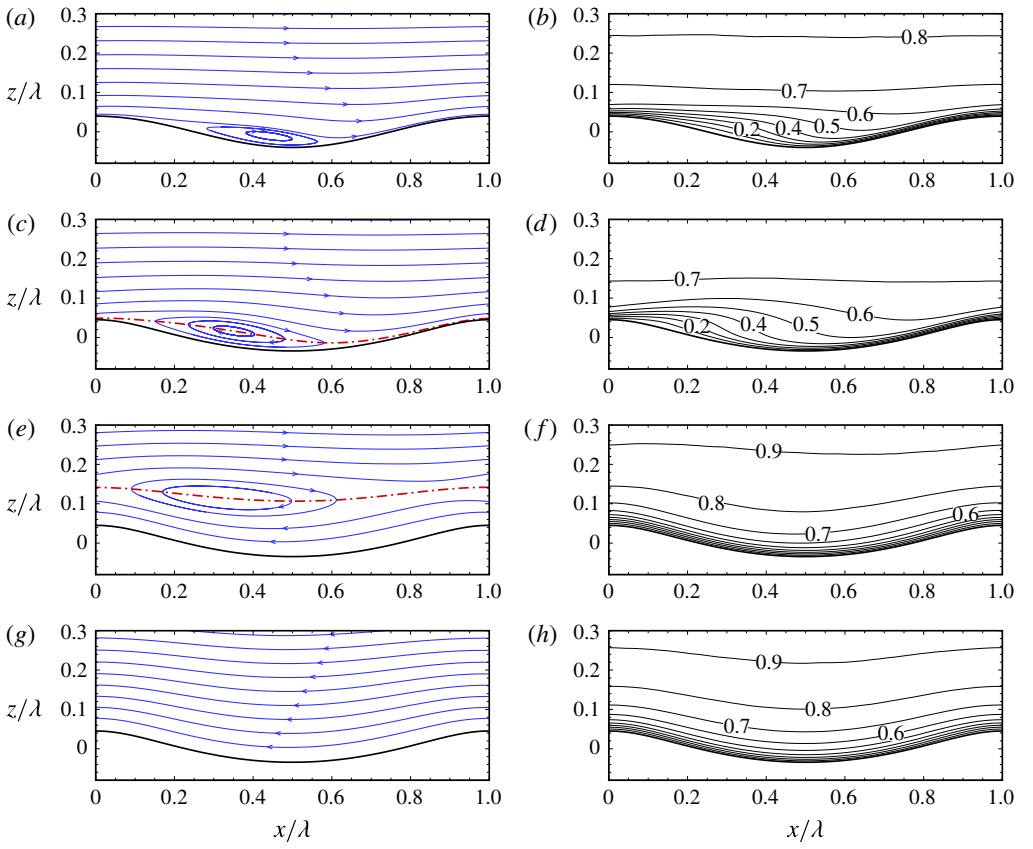

FIGURE 3. (Colour online) Phase-averaged (*a*,*c*,*e*,*g*) streamlines and (*b*,*d*,*f*,*h*) scalar concentration $\langle\theta\rangle$ (for $Sc = 1.0$) for various wave cases: (*a*,*b*) S25; (*c*,*d*) W25C2; (*e*,*f*) W25C14; and (*g*,*h*) W25C25. The streamlines are based on $(\langle u\rangle - c, \langle w\rangle)$, i.e. in the reference frame moving with the wave phase speed c. The red dash-dot line indicates the location of the critical layer where $\langle u\rangle - c = 0$ (it is located higher than $z/\lambda = 0.3$ in case W25C25 and thus is not shown in (*g*)). The contour interval for $\langle\theta\rangle$ is 0.1.

'cat's eye' by Lighthill (1962). For case W25C2, the cat's-eye streamlines are located right above the wave trough. Note that the cat's eyes pattern in figure 3(*c*) does not imply the occurrence of mean flow separation above the wave trough (see Banner & Melville 1976; Gent & Taylor 1977). Unlike in the flow over a stationary wave, in which a negative surface stress (i.e. reversed near-surface flow) would indicate a flow separation, in flows over progressive waves the near-surface flow is in the reversed direction in the wave-following reference frame everywhere above the wave surface. Yang & Shen (2010) used the local relative velocity (with respect to the local surface orbital velocity) and found occasional instantaneous flow separations occur on the leeward face of slow progressive waves, while the mean flow was found to remain unseparated. Similarly, in case W25C2 of the current DNS the mean flow is found to be unseparated. Compared with the mean flow separation bubble in case S25, in case W25C2 the cat's-eye streamline pattern extends further upwards and upstream, As a result, the low-$\langle\theta\rangle$ region above the wave trough is lifted further upwards, and this effect also extends further upstream when compared with case S25.

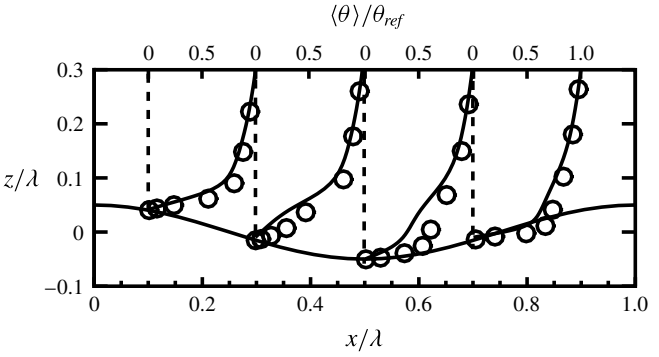

FIGURE 4. Comparison of phase-averaged scalar concentration $\langle\theta\rangle$ with $Sc = 0.7$ over a stationary wavy wall with steepness $ak = 0.314$. Profiles of $\langle\theta\rangle$ at $x/\lambda = 0.1$, 0.3, 0.5, and 0.7 are plotted: ∘, DNS of channel flow by Rossi (2010);——, current DNS with $Re_* = 283$. The reference value θ_{ref} for the normalization is based on the mean scalar concentration at $z = 0.3\lambda$.

For cases W25C14 (figure 3*e*,*f*) and W25C25 (figure 3*g*,*h*), the wave phase speed c is large and the critical layer is located far from the wave surface. Below the critical layer, the streamlines are nearly parallel to the wave surface with the mean streamwise velocity $\langle u\rangle - c$ in the $-x$-direction. Associated with this smooth streamline pattern, the contour lines for $\langle\theta\rangle$ are also nearly parallel to the wave surface. In cases W25C14 and W25C25 the scalar concentration $\langle\theta\rangle$ near the wave surface is in general higher than that in cases S25 and W25C2, as indicated by the lower elevations of the $\langle\theta\rangle = 0.6$ and 0.8 contour lines, respectively, in figures 3(*f*) and 3(*h*) compared with those in figures 3(*b*) and 3(*d*).

The effect of surface waves on the scalar field can be directly visualized from the distribution of the wave-induced variation of the scalar concentration, $\widetilde{\theta}$, in which the time and plane average $\overline{\theta}$ has been removed. Figure 5 shows the two-dimensional contours of $\widetilde{\theta}$ and the vertical profile of the ξ-average of its magnitude, $\overline{|\widetilde{\theta}|}$. For cases S25 (figure 5*a*) and W25C2 (figure 5*b*), the distribution of $\widetilde{\theta}$ is asymmetric about the wave crest, with negative values above the leeward face and trough, and positive values above the windward face and crest. For cases W25C14 (figure 5*c*) and W25C25 (figure 5*d*), the distribution of $\widetilde{\theta}$ becomes nearly symmetric with respect to the wave trough, with positive values above the trough and negative values above the crest. For all the four wave cases, the averaged magnitude $\overline{|\widetilde{\theta}|}$ has its maximum near the wave surface (at $\zeta/\lambda \lesssim 0.04$), and reduces to a small value at higher height. The peak values of $\overline{|\widetilde{\theta}|}$ for cases S25 and W25C2 are significantly higher than those for cases W25C14 and W25C25. Figure 5 also shows the effect of Sc on $\overline{|\widetilde{\theta}|}$. For all of the cases, the increase of Sc causes an increase of the peak value and a reduction in the height of the peak.

4.2. *Sherwood number*

The wave-induced variation of the near-surface scalar field causes considerable wave-correlated variation in the Sherwood number. The Sherwood number is usually used to measure the relative importance of convection and molecular diffusion in convective

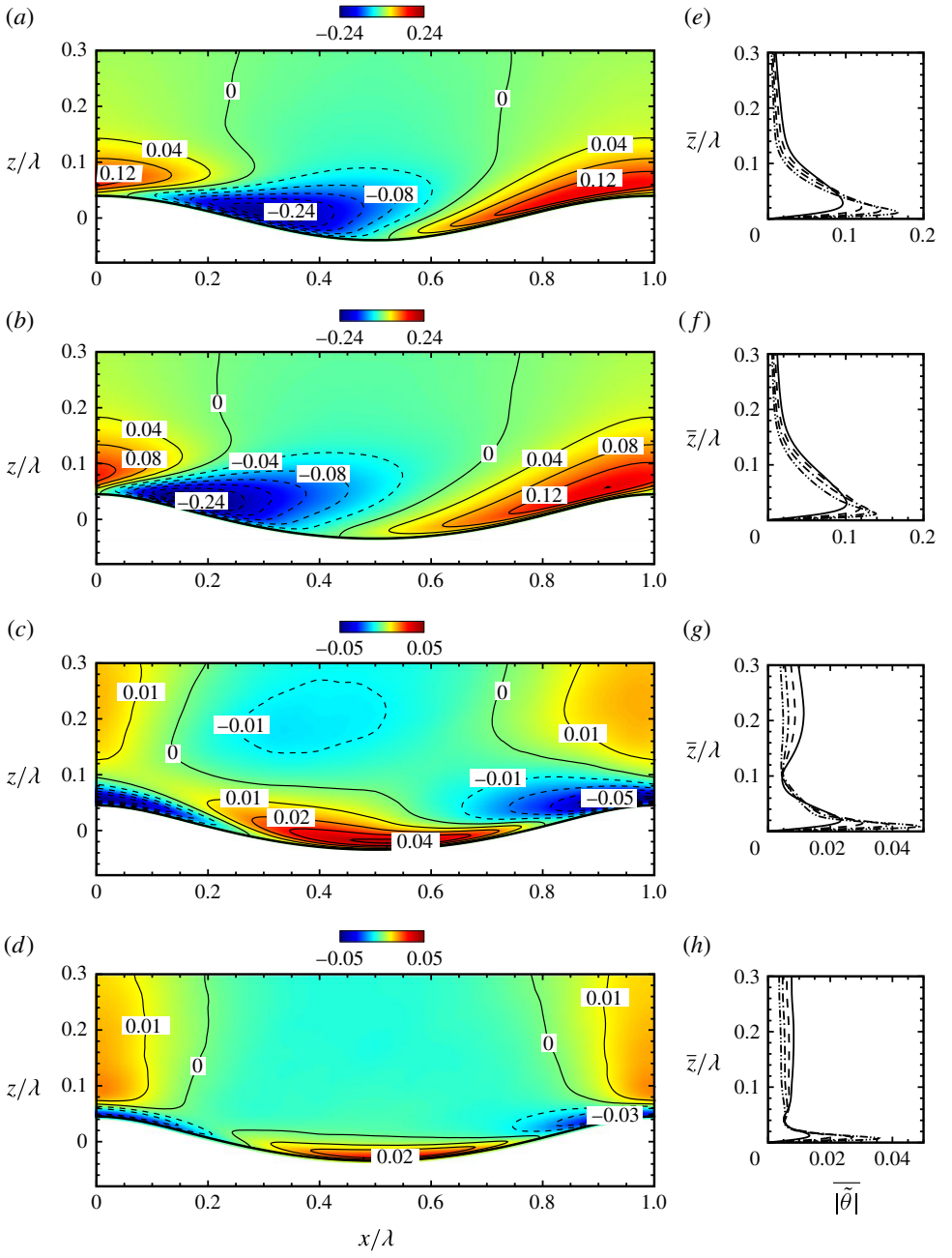

FIGURE 5. (Colour online) Distribution of wave-induced variation of scalar concentration, $\widetilde{\theta}$, for various wave cases: (*a*,*e*) S25; (*b*,*f*) W25C2; (*c*,*g*) W25C14; and (*d*,*h*) W25C25. (*a*–*d*) Show the contours of $\widetilde{\theta}$ for $Sc = 1.0$. The contour intervals are (*a*,*e*) 0.04, (*b*,*f*) 0.04, (*c*,*g*) 0.01 and (*d*,*h*) 0.01. Dashed contour lines indicate negative values. (*e*–*h*) Show the vertical profiles of $\overline{|\widetilde{\theta}|}$ (i.e. the average of $|\widetilde{\theta}|$ over all ξ) for various values of Sc: ——, $Sc = 0.5$; – – –, $Sc = 1.0$; — · —, $Sc = 2.0$; and — · · —, $Sc = 4.0$.

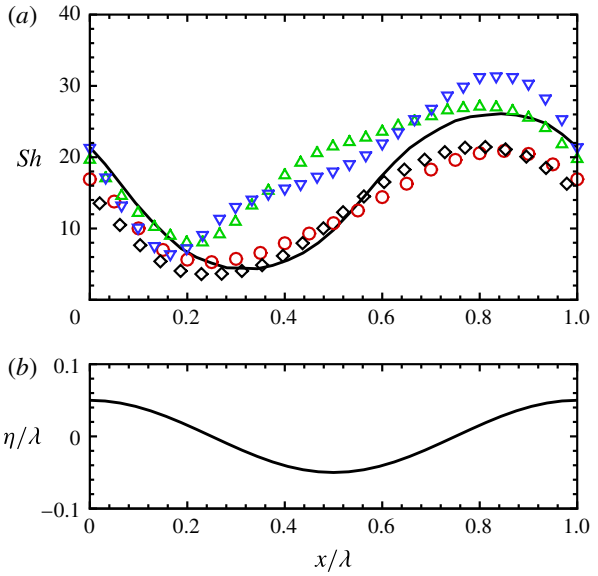

FIGURE 6. (Colour online) (*a*) Profiles of phase-averaged local Sherwood number *Sh* over the stationary wavy wall: ○, RANS result of Park *et al.* (2004) for $(ak, Sc) = (0.1\pi, 0.7)$; □, RANS result of Dellil *et al.* (2004) for $(ak, Sc) = (0.08\pi, 0.9)$; △, RANS result of Dellil *et al.* (2004) for $(ak, Sc) = (0.12\pi, 0.9)$; ▽, LES result of Choi & Suzuki (2005) for $(ak, Sc) = (0.1\pi, 0.7)$; and ——, current DNS result for $(ak, Sc) = (0.1\pi, 0.7)$ and $Re_* = 283$ (see figure 4). The corresponding wave surface phase is indicated by the wave elevation η of $ak = 0.1\pi$ in panel (*b*).

mass transfer processes (corresponding to the Nusselt number in heat transfer). The local Sherwood number along the wave surface based on the phase-averaged scalar field can be calculated as

$$Sh \equiv \frac{h\overline{H}/2}{D} = \frac{\left.\dfrac{\partial\langle\theta\rangle}{\partial z}\right|_{z=\eta}\overline{H}}{2(\overline{\theta}_{1/2} - \theta_0)}, \tag{4.2}$$

where h is the convective mass transfer coefficient, D is the molecular diffusivity as in (2.3), $\overline{\theta}_{1/2}$ is the averaged θ at the centre height of the domain ($\overline{z} = \overline{H}/2$), and $\theta_0 = 0$ is the imposed bottom surface value of θ as the boundary condition. Figure 6 shows the wave-correlated variation of *Sh* for the steep stationary wave case (i.e. the case with $ak = 0.314$ and $Re_* = 283$ as shown in figure 4), in which the current DNS result is compared with the results from several previous numerical studies (Park *et al.* 2004; Dellil *et al.* 2004; Choi & Suzuki 2005). For the steep stationary wave case, the profile of *Sh* has a nearly sinusoidal shape. On the stationary wavy surface, the value of *Sh* is small above the leeward face and large above the windward face, as a result of the smaller and larger vertical gradients of $\langle\theta\rangle$ on the leeward and windward faces, respectively, as shown in figures 3(*a*) and 4.

Figure 7 shows the effect of wave motion on *Sh*. The plotted curves are for $Sc = 1.0$. When the wave is slow (case W25C2), similar to the stationary wave condition, *Sh* is also small above the leeward face and large above the windward face. However, the

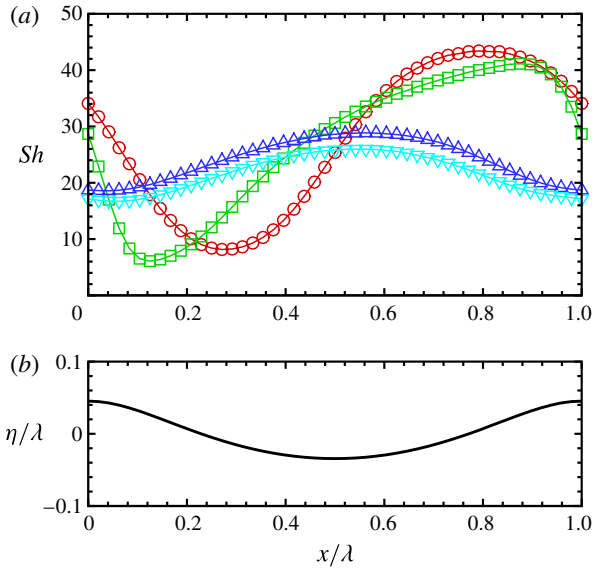

FIGURE 7. (Colour online) (*a*) Profiles of phase-averaged local Sherwood number Sh for $Sc = 1.0$ and for various wave cases: ○, S25 ($c/u_* = 0$); □, W25C2 ($c/u_* = 2$); △, W25C14 ($c/u_* = 14$); and ▽, W25C25 ($c/u_* = 25$). The corresponding wave surface phase is indicated by the wave elevation η in panel (*b*).

shape of the Sh curve apparently differs from the sinusoidal shape, with its minimum point closer to the wave crest (near $x/\lambda = 0.12$). For cases with intermediate (case W25C14) and fast (W25C25) waves, the distribution of Sh become symmetric with respect to the wave form, with the maxima above the wave trough and the minima above the crest, corresponding to the regions of positive and negative $\widetilde{\theta}$ in figure 5, respectively.

For a given wave condition, varying the Sc value mainly causes changes in the magnitudes of the mean and variation of Sh, while the shapes of the curves are similar to those of the corresponding curves shown in figure 7. Thus, these additional Sh curves with different Sc are not plotted here, and only the effect of Sc on the averaged Sherwood number $\overline{Sh}$ $(= (1/\lambda)\int_0^\lambda Sh(x)\mathrm{d}x)$ is discussed. Figure 8 shows the dependence of $\overline{Sh}$ on Sc. Previous studies on scalar transport in wall-bounded or free-surface-bounded turbulent flows have shown that the scaling of $\overline{Sh}$ with Sc follows a power law (e.g. Shaw & Hanratty 1977; Jähne & Haußecker 1998; Na, Papavassiliou & Hanratty 1999; Hasegawa & Kasagi 2008), i.e.

$$\overline{Sh} = \alpha Sc^{\beta}. \tag{4.3}$$

The current DNS results also exhibit this power-law trend for each wave condition as shown in figure 8. For the four different surface wave conditions considered in this study, the power-law coefficient β varies slightly around an averaged value of 0.555, while α varies between 21.13 and 27.09. The pronounced variation of α with the surface wave condition indicates the importance of wave motion on the magnitude of scalar transport. To further elucidate the effect of wave motion on scalar transport, the averaged Sherwood number $\overline{Sh}$ is plotted in figure 9 as a function of the wave

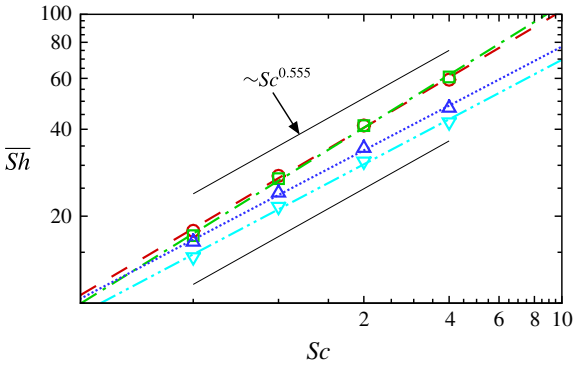

FIGURE 8. (Colour online) Dependence of mean Sherwood number $\overline{Sh}$ on Sc for various wave cases: ○, S25 ($c/u_* = 0$); □, W25C2 ($c/u_* = 2$); △, W25C14 ($c/u_* = 14$); and ▽, W25C25 ($c/u_* = 25$). The lines are the curve fittings: – – –, $\overline{Sh} = 27.09Sc^{0.579}$ for S25; — · —, $\overline{Sh} = 26.54Sc^{0.609}$ for W25C2; · · · , $\overline{Sh} = 23.68Sc^{0.514}$ for W25C14; and — · · —, $\overline{Sh} = 21.13Sc^{0.518}$ for W25C25. The two solid lines show the averaged slope of the four surface wave conditions, i.e. $\overline{Sh} \propto Sc^{0.555}$.

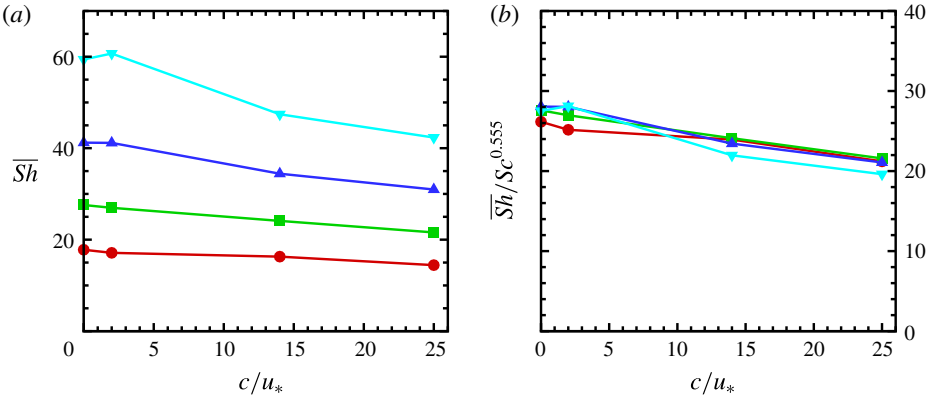

FIGURE 9. (Colour online) Dependence of mean Sherwood number $\overline{Sh}$ on wave age c/u_* for various Schmidt numbers: –●–, $Sc = 0.5$; –■–, $Sc = 1.0$; –▲–, $Sc = 2.0$; and –▼–, $Sc = 4.0$. In panel (*b*), $\overline{Sh}$ is rescaled by $Sc^{0.555}$.

age c/u_*. When Sc is fixed, in general $\overline{Sh}$ decreases as c/u_* increases (figure 9*a*). When normalized by $Sc^{0.555}$ (as suggested by the curve fitting in figure 8), the $\overline{Sh}$ curves for all the different Schmidt numbers collapse reasonably well.

4.3. *Profiles of time- and plane-averaged quantities*

The phase-averaged statistics in § 4.1 have shown significant wave-induced variation in the scalar field, which is highly dependent on the wave phase. In many practical applications, the surface wave effect is usually not directly captured in a phase-resolved context. Instead, the averaged wave effect is parameterized as the effective wave roughness that appears in the one-dimensional profiles of the time- and plane-averaged velocity and scalar concentration, which can be obtained based on field and laboratory measurement data (e.g. Charnock 1955; Smith 1988;

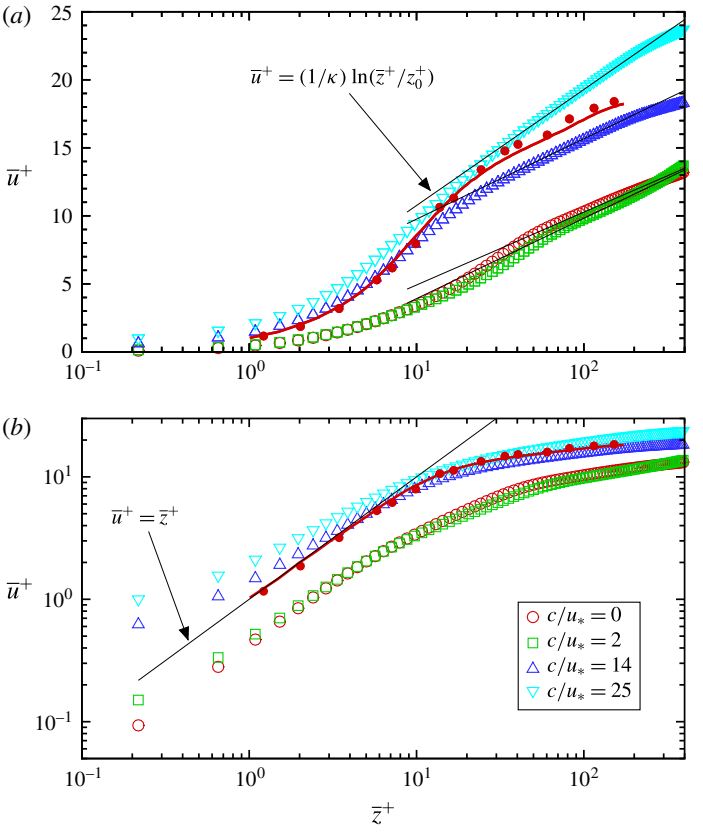

FIGURE 10. (Colour online) Profiles of mean streamwise velocity $\overline{u}^+$ for various wave cases: ○, S25 ($c/u_* = 0$); □, W25C2 ($c/u_* = 2$); △, W25C14 ($c/u_* = 14$); and ▽, W25C25 ($c/u_* = 25$). The semi-logarithmic plot in panel (*a*) highlights the log-law region, with the thin solid lines indicating the logarithmic law $\overline{u}^+ = (1/\kappa)\ln(\overline{z}^+/z_0^+)$ and the corresponding values of κ and z_0^+ for each simulation case given in table 1. The logarithmic plot in panel (*b*) highlights the near-wall viscous layer, with the thin solid lines indicating the linear law $\overline{u}^+ = \overline{z}^+$. In the figure, the DNS result of flat-boundary channel flow from Kim, Moin & Moser (1987) is indicated by the thick line, and the experimental data from Eckelmann (1974) (corrected by Kim *et al.* 1987) are indicated by the filled circles.

Fairall *et al.* 1996; Johnson *et al.* 1998; Toba *et al.* 2001). Although limited to low Reynolds number conditions, DNS has been shown to provide valuable insights for understanding the dependence of the effective wave roughness on the characteristics of the waves (Sullivan *et al.* 2000). In this subsection, time and plane averaging is performed for the instantaneous snapshots of scalar and velocity fields obtained from the current DNS to help quantify the averaged wave effect. Note that the plane average is performed on the ζ-plane in the computational space, as defined in § 4.1.

Figure 10 shows the profiles of the mean streamwise velocity $\overline{u}$ (for the definition, see (4.1) and the associated discussion). The slow wave case (W25C2, $c/u_* = 2$) shows a mean velocity profile close to that of the stationary wave case (S25). As c/u_* increases, the profile of $\overline{u}^+$ shifts monotonically towards higher values, which is expected since the wave form drag decreases as c/u_* increases (Belcher & Hunt 1998). For the current DNS, the normalized pressure-induced form drag F_p and surface

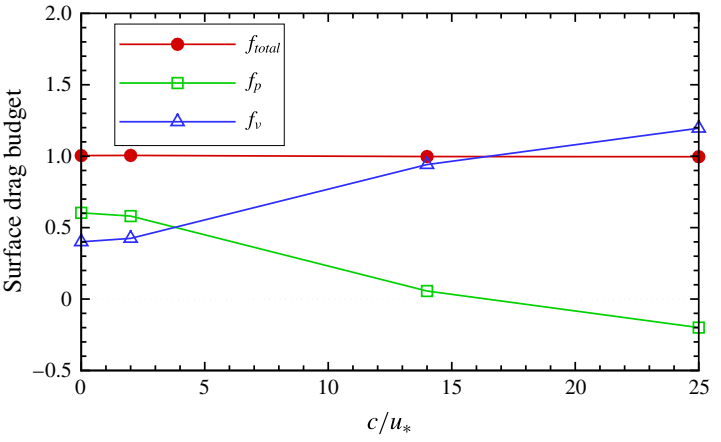

FIGURE 11. (Colour online) Budget of surface drag as a function of wave age: —●—, total surface drag f_{total};—□—, pressure-induced form drag f_p; and —△—, viscous drag f_v.

viscous drag F_v per unit projected horizontal area can be calculated based on the phase-averaged pressure and velocity as

$$F_p = \frac{1}{u_*^2 \lambda} \int_0^\lambda \frac{\langle p \rangle}{\rho} \frac{\partial \eta}{\partial x} \, \mathrm{d}x, \tag{4.4}$$

$$F_v = \frac{1}{u_*^2 \lambda} \int_0^\lambda \nu \left[\left(\frac{\partial \langle u \rangle}{\partial z} + \frac{\partial \langle w \rangle}{\partial x} \right) - 2 \frac{\partial \langle u \rangle}{\partial x} \frac{\partial \eta}{\partial x} \right] \mathrm{d}x, \tag{4.5}$$

and the total surface drag per unit area equals to their sum, $F_{total} = F_p + F_v$. As shown in figure 11, in cases S25 and W25C2, the form drag makes a significant contribution to the total surface drag. In case W25C14, the form drag is very small and the total surface drag is mostly due to the viscous effect, indicating that the mean flow and the surface wave are nearly in equilibrium. In case W25C25, the wave phase speed is fast and the surface wave pushes the mean flow forwards, resulting in negative form drag (i.e. a thrust). A similar dependence of the surface drag on the wave age has been reported in various previous studies (e.g. Li *et al.* 2000; Sullivan *et al.* 2000; Kihara *et al.* 2007; Yang & Shen 2010).

For all the four wave conditions considered in this study, the mean velocity profiles exhibit a distinct logarithmic region, as indicated by the thin solid lines in the semi-logarithmic plot in figure 10(*a*). These lines are determined by fitting the mean velocity profiles in the range of $\overline{z}^+ \in [50, 150]$ (see appendix B) with the logarithmic profile

$$\overline{u}^+ = \frac{1}{\kappa} \ln \left(\overline{z}^+ / z_0^+ \right) = \frac{1}{\kappa} \ln(\overline{z}^+) + B, \tag{4.6}$$

where the superscript '+' denotes the quantities normalized by the wall units (i.e. velocity is normalized by u_* and length is normalized by ν/u_*), κ is the von Kármán constant, z_0^+ is the effective wave surface roughness, and B is the profile offset. For each case, the corresponding log-law profile parameters κ, z_0^+ and B are listed in table 1. Similar to the DNS results reported in Sullivan *et al.* (2000), the evaluated z_0^+ values in most of the DNS cases considered in this study fall in the transitional regime ($0.1 < z_0^+ < 2.2$) in terms of the sea-surface roughness, which was

categorized to be a common sea state by Kitaigorodskii & Donelan (1984). The slow wave case W25C2 exhibits a roughness of $z_0^+ = 2.31$ that is slightly higher than the upper bound of the transitional regime. For cases S25, W25C2 and W25C14, the values for κ are close to the standard value of $\kappa = 0.41$ for the flat-wall case. The fast wave case W25C25 exhibits a smaller value of $\kappa = 0.27$, which is likely due to the strong surface motion of the fast propagating surface waves when $c/u_* = 25$. Similarly, Sullivan *et al.* (2000) reported a 10 % reduction of κ in DNS of turbulence over progressive waves with $ak = 0.1$ (i.e. the waves are less steep than the ones studied here). Note that due to this smaller κ in case W25C25, its evaluated z_0^+ is larger than that in case W25C14. Therefore, the larger z_0^+ in case W25C25 does not imply that the turbulence sees the fast wave 'rougher' than the intermediate wave. It should be pointed out that caution should be taken when interpreting the mean velocity profile for the present fast wave case due to the limited Reynolds number used in this study. Under real oceanic conditions, the fast wave case usually corresponds to the wind over storm-generated ocean swells, for which the Reynolds number is much higher than what a DNS can afford. The current DNS of $c/u_* = 25$ are more relevant to the condition of light wind over fast mechanically generated waves in laboratory-scale wind–wave tanks (e.g. Buckley & Veron 2016). Further study is required in the future in order to understand the effect of surface waves on the von Kármán constant and the wave surface roughness.

The near-surface behaviour of the mean velocity profile is shown by the logarithmic plot in figure 10(*b*). The mean velocity profiles exhibit a nearly linear behaviour in the viscous sublayer (i.e. $\overline{z}^+ < 5$), with some non-negligible difference from the linear law of the flat-wall turbulence. In particular, the viscous sublayer profiles of the intermediate (W25C14) and fast (W25C25) wave cases are close to the linear profile of the flat-wall case (e.g. Kim *et al.* 1987; Lee & Moser 2015), i.e. $\overline{u}^+ = \overline{z}^+$, but with larger value towards the wave surface due to the positive mean streamwise surface orbital velocity of the nonlinear Stokes wave. On the other hand, the stationary (S25) and slow (W25C2) wave cases also show a linear profile in the viscous sublayer, but with a velocity deficit compared with the flat-wall linear law. The viscous sublayer profile of the stationary wave case (S25) is nearly parallel to that of the flat wall, while the one for the slow wave case (W25C2) is tilted slightly towards higher values when approaching the surface due to the positive mean surface orbital velocity of the Stokes waves.

A similar analysis can be done for the mean scalar concentration. By compiling a number of experimental datasets, Kader (1981) showed that the mean temperature and scalar concentration in fully developed turbulent boundary layers follow a linear profile in the viscous sublayer and a logarithmic profile in the log-law region. In the near-surface region, the Kader correlation suggests that

$$\overline{\theta}^+/Sc = \overline{z}^+ - Sc[c_4\overline{z}^{+4} + O(\overline{z}^{+5})], \tag{4.7}$$

where $c_4 \approx 1.5 \times 10^{-4}$ as estimated based on the experimental data (Kader 1981). Therefore, for the flat-wall case it is expected that

$$\overline{\theta}^+ \approx Sc\,\overline{z}^+ \tag{4.8}$$

to the leading order near the surface, with the deviation from this linear profile increasing towards larger $\overline{z}^+$ and with higher Sc. Similar near-surface linear behaviour is found in the current DNS results over wave surfaces. Here $\overline{\theta}^+ = \overline{\theta}/\theta_*$, where

$$\theta_* = \frac{D}{u_*}\frac{\mathrm{d}\overline{\theta}}{\mathrm{d}\overline{z}}\bigg|_{\overline{z}=0} \tag{4.9}$$

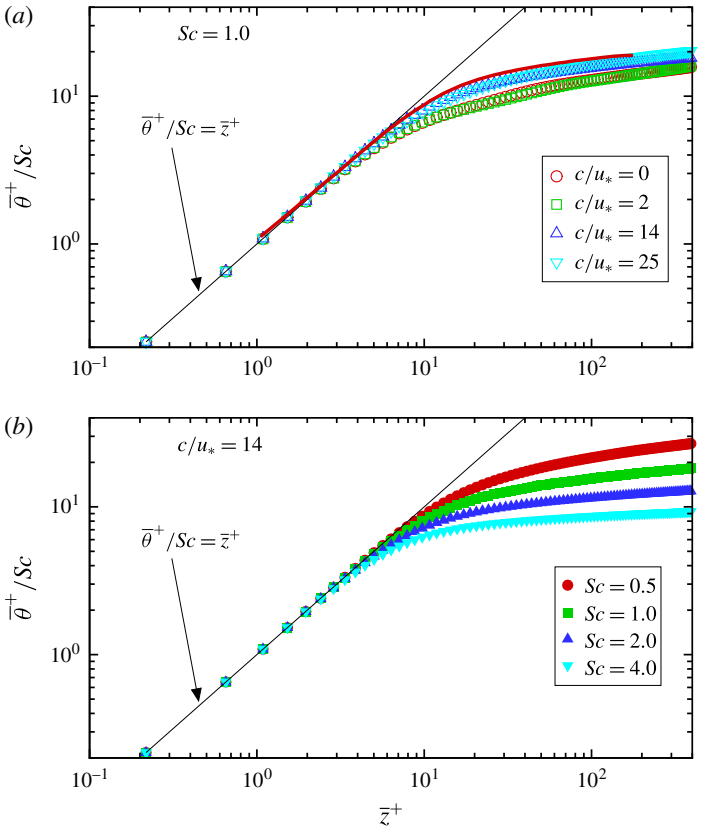

FIGURE 12. (Colour online) Profiles of rescaled mean scalar concentration $\overline{\theta}^+/Sc$. Panel (*a*) shows various wave cases with a fixed Schmidt number $Sc = 1.0$: ○, S25 ($c/u_* = 0$); □, W25C2 ($c/u_* = 2$); △, W25C14 ($c/u_* = 14$); and ▽, W25C25 ($c/u_* = 25$). Panel (*b*) shows case W25C14 ($c/u_* = 14$) with various Schmidt numbers: ●, $Sc = 0.5$; ■, $Sc = 1.0$; ▲, $Sc = 2.0$; and ▼, $Sc = 4.0$. The profiles are shown on a logarithmic scale to highlight the near-wall region, with the solid line indicating the linear law $\overline{\theta}^+/Sc = \overline{z}^+$. In panel (*a*), the DNS result from Kawamura *et al.* (1998) is also plotted (the thick line).

is a characteristic scalar scale (in the case of heat transfer, θ_* is also referred to as the friction temperature) (Kim & Moin 1989). Figure 12 shows the profiles of $\overline{\theta}^+/Sc$ (in a logarithmic plot) for some representative cases obtained by the current DNS. In particular, figure 12(*a*) shows the profiles for various wave cases with $Sc = 1.0$, and figure 12(*b*) shows the profiles for case W25C14 with various Schmidt numbers (other cases also follow consistent trends for the wave and Sc dependences, and are thus not shown here due to space limitation). In the viscous sublayer ($\overline{z}^+ < 5$), the profiles for different wave conditions and Schmidt numbers collapse well and agree with the linear law found in the flat-wall condition.

The logarithmic law behaviour of $\overline{\theta}^+$ can be visualized in a semi-logarithmic plot as shown in figure 13. Similar to the profile of $\overline{u}^+$, for a fixed Sc the $\overline{\theta}^+$ profile shifts towards higher values when c/u_* increases, with the profile for $c/u_* = 2$ close to that for the stationary wave case (figure 13*a*). For each wave condition, the $\overline{\theta}^+$ profile shifts monotonically to higher values when Sc increases (see for example the

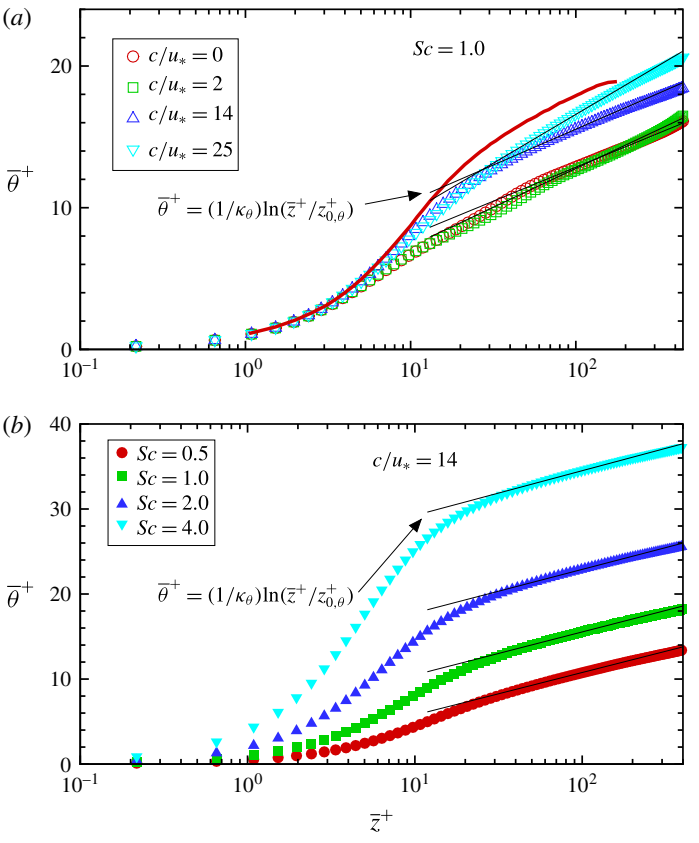

FIGURE 13. (Colour online) Profiles of mean scalar concentration $\overline{\theta}^+$. The definitions of the symbols are the same as those in figure 12. The profiles are shown on a semi-logarithmic scale to highlight the log-law region, with the thin solid lines indicating the logarithmic law $\overline{\theta}^+ = (1/\kappa_\theta)\ln(\overline{z}^+/z^+_{0,\theta})$ and the corresponding values of κ_θ and $z^+_{0,\theta}$ for each simulation case given in table 1. In panel (*a*), the DNS result from Kawamura *et al.* (1998) is also plotted (the thick line).

case W25C14 shown in figure 13*b*). Similar to (4.6), the logarithmic law for scalar concentration can be written as (e.g. Kader 1981)

$$\overline{\theta}^+ = \frac{1}{\kappa_\theta}\ln(\overline{z}^+/z^+_{0,\theta}) = \frac{1}{\kappa_\theta}\ln\overline{z}^+ + B_\theta, \tag{4.10}$$

where κ_θ is the von Kármán constant of scalar, $z^+_{0,\theta}$ is the effective wave surface roughness for scalar, and B_θ is the offset of the mean scalar profile. For each wave case, the corresponding parameters κ_θ, $z^+_{0,\theta}$, and B_θ can be obtained by fitting the DNS data in the log-law region (defined as $50 < z^+ < 150$ in this study as explained in appendix B) with the logarithmic profile (4.10). The estimated values of these parameters are listed in table 1. For each wave case, the evaluated value of the scalar von Kármán constant κ_θ exhibits a small variation when the Schmidt number is changed, while the profile offset B_θ (or the roughness $z^+_{0,\theta}$) increases significantly as Sc increases.

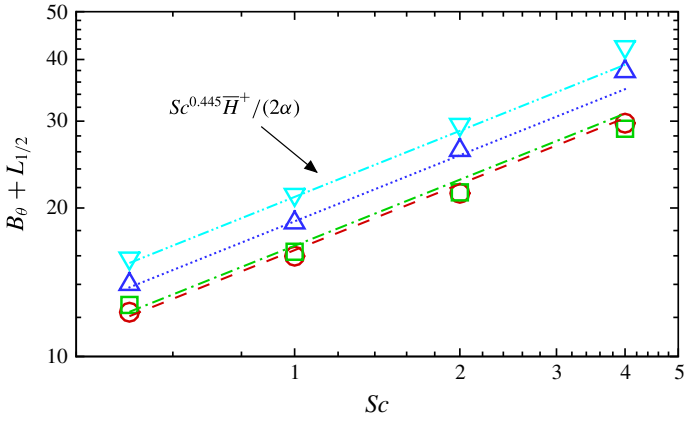

FIGURE 14. (Colour online) Dependence of B_θ on the Schmidt number for various wave cases: ○, S25 ($c/u_* = 0$); □, W25C2 ($c/u_* = 2$); △, W25C14 ($c/u_* = 14$); and ▽, W25C25 ($c/u_* = 25$). Equation (4.14) suggests that $B_\theta + L_{1/2} = Sc^{1-\beta}\overline{H}^+/(2\alpha)$, as shown by the lines: – – –, S25; — · —, W25C2; · · · , W25C14; and — · · —, W25C25. For the current DNS, $\beta \approx 0.555$ when averaged among the four wave conditions, and the α value for each wave condition can be found in the caption of figure 8.

The dependence of B_θ on Sc can be further quantified. Recall that the averaged Sherwood number $\overline{Sh}$ follows a power-law dependence on Sc, as shown in (4.3). Applying the surface average to (4.2) and combining it with (4.3) yields

$$\alpha Sc^{\beta} = \left.\frac{\mathrm{d}\overline{\theta}^+}{\mathrm{d}\overline{z}}\right|_{\overline{z}^+=0} \frac{\overline{H}^+}{2\overline{\theta}^+_{1/2}}. \tag{4.11}$$

The near-surface linear profile (4.8) gives

$$\left.\frac{\mathrm{d}\overline{\theta}^+}{\mathrm{d}\overline{z}}\right|_{\overline{z}^+=0} = Sc, \tag{4.12}$$

and the logarithmic profile (4.10) gives

$$\overline{\theta}^+_{1/2} = \frac{1}{\kappa_\theta}\ln\left(\overline{H}^+/2\right) + B_\theta. \tag{4.13}$$

Substituting (4.12) and (4.13) into (4.11) gives

$$B_\theta = \frac{\overline{H}^+}{2\alpha} Sc^{1-\beta} - L_{1/2}, \tag{4.14}$$

where

$$L_{1/2} = \frac{1}{\kappa_\theta}\ln\left(\overline{H}^+/2\right). \tag{4.15}$$

As shown in table 1 and figure 9, for a given wave condition the parameters α, β and κ_θ estimated based on the current DNS data are nearly constant. Therefore, equation (4.14) suggests that $B_\theta \sim Sc^{1-\beta}$, where $\beta \approx 0.555$ as shown in § 4.2. Figure 14 shows the estimated $B_\theta + L_{1/2}$ as a function of the Schmidt number. With $\beta = 0.555$ and α given by the power-law fitting in figure 8, equation (4.14) is found to provide a reasonable parameterization for B_θ, which agrees well with the B_θ values obtained directly from the log-law profile fitting (the values are listed in table 1).

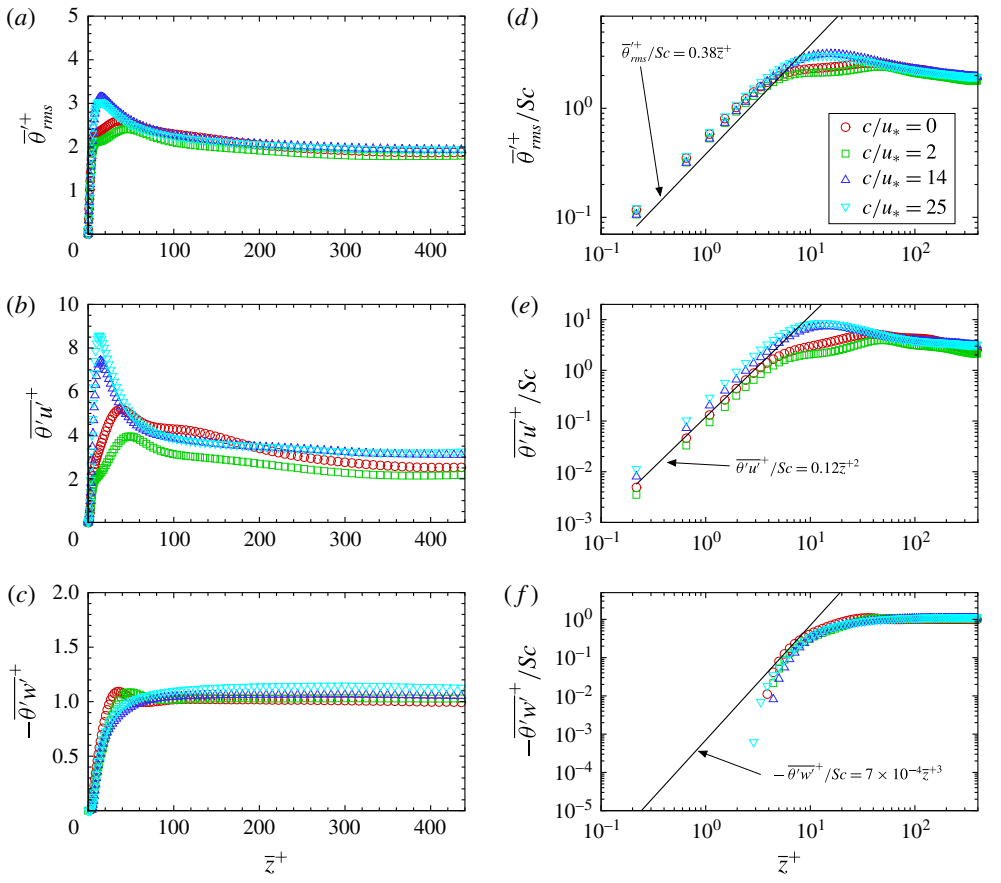

FIGURE 15. (Colour online) Profiles of (*a*) $\overline{\theta'}^{+}_{rms}$, (*b*) $\overline{\theta'u'}^{+}$, and (*c*) $\overline{-\theta'w'}^{+}$ on a linear scale; and profiles of (*d*) θ'^{+}_{rms}/Sc, (*e*) $\overline{\theta'u'}^{+}/Sc$, and (*f*) $\overline{-\theta'w'}^{+}/Sc$ on a logarithmic scale. The plotted DNS results are for $Sc = 1.0$ with various wave cases: ○, S25 ($c/u_* = 0$); □, W25C2 ($c/u_* = 2$); △, W25C14 ($c/u_* = 14$); and ▽, W25C25 ($c/u_* = 25$). The solid lines in (*d–f*) indicate the expressions proposed by Kawamura *et al.* (1998).

4.4. *Time- and plane-averaged statistics of scalar fluctuations*

The presence of surface waves can induce a strong effect on the air turbulence. Statistics of velocity fluctuations above plane progressive waves of various wave ages and steepnesses have been studied in detail in previous studies (e.g. Sullivan *et al.* 2000; Kihara *et al.* 2007; Sullivan *et al.* 2008; Yang & Shen 2010; Hara & Sullivan 2015). On the other hand, the statistics of scalar fluctuations over waves have rarely been studied, with the exception of some studies for stationary wavy walls (e.g. Dellil *et al.* 2004; Park *et al.* 2004; Rossi 2010) and for stratified turbulence over water waves (e.g. Sullivan & McWilliams 2002; Druzhinin *et al.* 2016).

In this subsection, the time- and plane-averaged statistics of scalar fluctuations are studied based on the DNS data. Figure 15(*a–c*) shows the profiles of $\overline{\theta'}^{+}_{rms}$, $\overline{\theta'u'}^{+}$, and $\overline{-\theta'w'}^{+}$ for various wave cases with $Sc = 1.0$. The profiles of $\overline{\theta'}^{+}_{rms}$ (figure 15*a*) and $\overline{\theta'u'}^{+}$ (figure 15*b*) have a similar trend. As $\overline{z}^{+}$ increases from 0, the value first increases to a peak and then decreases to approach a constant value. In particular,

the maximum is at $\bar{z}^+ \approx 35$ for case S25, $\bar{z}^+ \approx 47$ for case W25C2, and $\bar{z}^+ \approx 15$ for cases W25C14 and W25C25. Among the three progressive wave cases, the peak values of both $\overline{\theta'^2}^+_{rms}$ and $\overline{\theta'u'}^+$ increase with c/u_*, indicating the increase of wave effect as the wave propagates faster. The peak values of $\overline{\theta'^2}^+_{rms}$ and $\overline{\theta'u'}^+$ in case S25 are slightly higher than the corresponding ones in case W25C2, because the presence of flow separation in case S25 (figure 3*a*) enhances the turbulence intensity above the wave trough. The wave-induced effect on $\overline{\theta'^2}^+_{rms}$ and $\overline{\theta'u'}^+$ appears to be mainly in the viscous wall region (i.e. $\bar{z}^+ < 50$), with only slight differences at higher elevation.

Figure 15(*c*) shows the profiles of $\overline{-\theta'w'}^+$. Assuming a statistically steady state and integrating the scalar transport equation over a control volume, the total vertical scalar flux at any height z,

$$\overline{-\theta'w'} + D\frac{\mathrm{d}\bar{\theta}}{\mathrm{d}\bar{z}} = \theta_* u_*, \tag{4.16}$$

is a constant in the stress-driven Couette flow considered in the present study. In the viscous wall region ($\bar{z}^+ < 50$), the contribution from the molecular flux $D\mathrm{d}\bar{\theta}/\mathrm{d}\bar{z}$ is significant, therefore the value of $\overline{-\theta'w'}^+$ ($= \overline{-\theta'w'}/\theta_* u_*$) is less than 1. In this region, the values of $\overline{-\theta'w'}^+$ in cases S25 and W25C2 are larger than those in cases W25C14 and W25C25. In the outer region ($\bar{z}^+ > 50$), the molecular diffusion effect is negligible and thus $\overline{-\theta'w'}^+ \approx 1.0$ for all of the cases. Similar to $\overline{\theta'^2}^+_{rms}$ and $\overline{\theta'u'}^+$, the profile of $\overline{-\theta'w'}^+$ is also affected by the surface waves mainly in the viscous wall region. In particular, as $\bar{z}^+$ increases, $\overline{\theta'u'}^+$ approaches 1 more rapidly in cases S25 and W25C2 than in cases W25C14 and W25C25, indicating more intensive turbulent mixing in cases S25 and W25C2.

Previous studies on scalar transport over flat boundary have shown that in the viscous sublayer (i.e. $\bar{z}^+ < 5$) the scalar fluctuation profiles can be expressed (to the leading order) as (e.g. Antonia & Kim 1991; Kawamura *et al.* 1998)

$$\overline{\theta'^2}^+_{rms}/Sc = 0.38\bar{z}^+, \tag{4.17}$$

$$\overline{\theta'u'}^+/Sc = 0.12\bar{z}^{+2}, \tag{4.18}$$

$$\overline{-\theta'w'}^+/Sc = 7\times 10^{-4}\bar{z}^{+3}. \tag{4.19}$$

To look closely at the viscous sublayer, we plot in figure 15(*d–f*) the profiles of $\overline{\theta'^2}^+_{rms}/Sc$, $\overline{\theta'u'}^+/Sc$, and $\overline{-\theta'w'}^+/Sc$ on a logarithmic scale. For $\overline{\theta'^2}^+_{rms}/Sc$ and $\overline{\theta'u'}^+/Sc$, the DNS results for various wave cases are found to be close to the expressions given by (4.17) and (4.18), respectively. Differently, for $\overline{-\theta'w'}^+/Sc$ the presence of waves causes an obvious discrepancy from the flat-wall expression given by (4.19). For better understanding of the effect of surface waves on the vertical scalar flux $-\theta'w'$, more turbulence statistics are quantified and discussed later in §§ 4.5 and 4.6.

Figure 16 shows the effect of Sc on the time- and plane-averaged statistics of scalar fluctuation and fluxes. In particular, figure 16(*a–c*) shows the profiles of $\overline{\theta'^2}^+_{rms}$, $\overline{\theta'u'}^+$, and $\overline{-\theta'w'}^+$ for the wave case W25C14 with various Sc. For $\overline{\theta'^2}^+_{rms}$ (figure 16*a*) and $\overline{\theta'u'}^+$ (figure 16*b*), when Sc increases, their peaks in the viscous wall region (i.e. $\bar{z}^+ < 50$) increase significantly, while in the outer layer (i.e. $\bar{z}^+ > 50$) the profiles only slightly shift towards larger values. When rescaled by Sc and plotted on a logarithmic scale, in the viscous sublayer (i.e. $\bar{z}^+ < 5$) the profiles of $\overline{\theta'^2}^+_{rms}/Sc$ (figure 16*d*) and $\overline{\theta'u'}^+/Sc$ (figure 16*e*) for all of the four Sc values are close to the expressions given by (4.17) and (4.18), respectively. Differently, the change of Sc has much less effect on the profile of $\overline{-\theta'w'}^+$ (figure 16*c*). When plotted on a logarithmic scale (figure 16*f*),

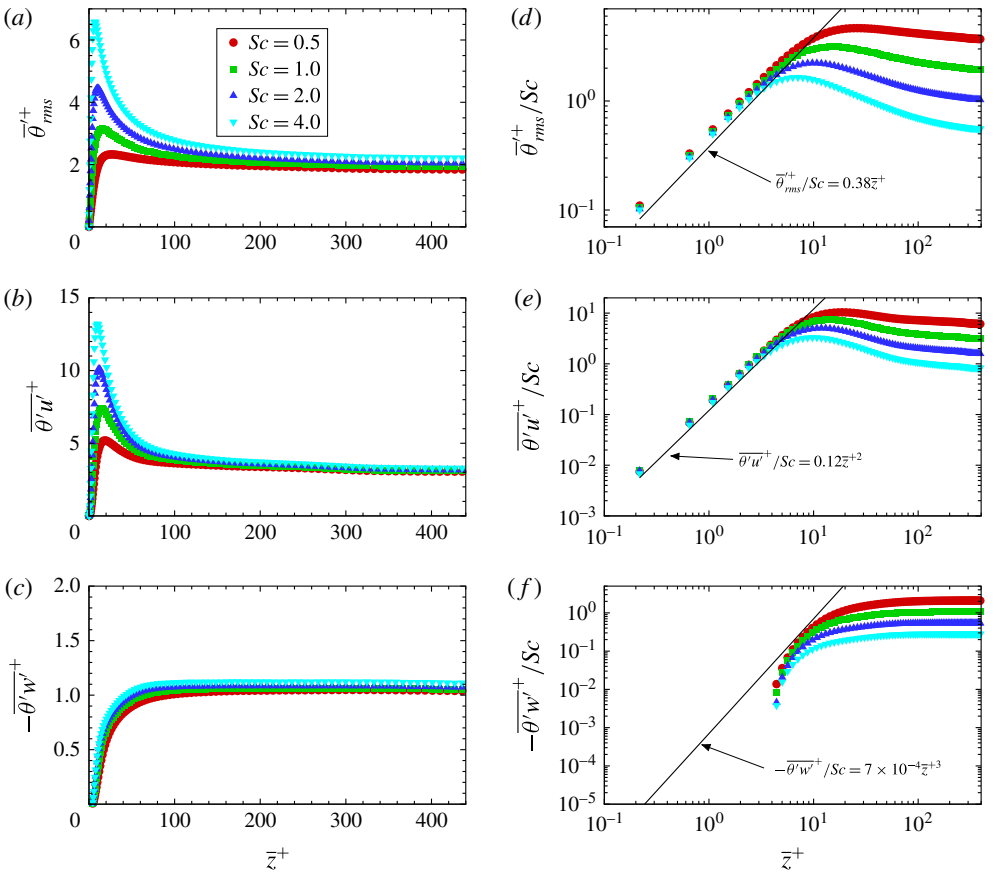

FIGURE 16. (Colour online) Profiles of (*a*) $\overline{\theta}^{+}_{rms}$, (*b*) $\overline{\theta' u'}^{+}$, and (*c*) $\overline{-\theta' w'}^{+}$ on a linear scale; and profiles of (*d*) θ^{+}_{rms}/Sc, (*e*) $\overline{\theta' u'}^{+}/Sc$, and (*f*) $\overline{-\theta' w'}^{+}/Sc$ on a logarithmic scale. The plotted DNS results are for the wave case W25C14 with various Schmidt numbers: –●–, $Sc = 0.5$; –■–, $Sc = 1.0$; –▲–, $Sc = 2.0$; and –▼–, $Sc = 4.0$. The solid lines in (*d–f*) indicate the expressions proposed by Kawamura *et al.* (1998).

the profiles of $\overline{-\theta' w'}^{+}/Sc$ differ significantly from the flat-wall expression given by (4.19), similar to the results shown in figure 15(*f*).

In figures 15 and 16, only a number of selected cases are shown to illustrate the effect of surface waves and Schmidt number on the statistics of scalar fluctuations. Other cases exhibit similar trends for the surface wave and Sc effects. Note that in the logarithmic plots shown in figures 15(*f*) and 16(*f*), for most of the cases the viscous sublayer portion of the $\overline{-\theta' w'}^{+}/Sc$ profile cannot be displayed because $\overline{-\theta' w'}^{+}/Sc < 0$ there, which is caused by the strong wave-induced modulation to the vertical scalar flux $-\theta' w'$. About this point, more discussions are given in §§ 4.5 and 4.6.

4.5. *Wave-correlated distribution of scalar variance and fluxes*

To help understand the effect of surface waves on the scalar fluctuation statistics, in this subsection the phase averaging method (see § 4.1 for the mathematical definition) is used to quantify the wave-correlated distribution of the scalar variance and fluxes.